Research Article | Vol. 31, No. 17 / 14 Aug 2023 / Optics Express 28636
Optics EXPRESS

Signal processing integrated with fiber-optic Vernier effect for the simultaneous measurement of relative humidity and temperature

YU WANG,[1] WEIHAO YUAN,[1] YAXI YAN,[2,4] ZHENGGANG LIAN,[3] DARU CHEN,[2,5] ALAN PAK TAO LAU,[1] CHANGYUAN YU,[1] AND CHAO LU[1]

[1]*Photonics Research Institute, Department of Electrical and Electronic Engineering, Hong Kong Polytechnic University, Hong Kong, China*
[2]*Hangzhou Institute of advanced studies, Zhejiang Normal University, Hangzhou, China*
[3]*Yangtze Optical Electronics Co., Ltd. (YOEC), East Lake Hi-Tech Develop zone, Wuhan, China*
[4]*ya.xi.yan@connect.polyu.hk*
[5]*daru@zjnu.cn*

Abstract: A novel inline Fabry-Perot interferometer (FPI) for simultaneous relative humidity (RH) and temperature monitoring is proposed. The sensing probe consists of a section of hollow core Bragg fiber (HCBF) spliced with a single-mode fiber pigtail. The end-face of the HCBF is coated with Chitosan and ultraviolet optical adhesive (UVOA), forming two polymer layers using a well-designed fabrication process. The surfaces of the layers and splicing point will generate multiple-beam interference and form Vernier-effect (VE) related envelopes in the reflection spectrum. A signal processing (SP) method is proposed to demodulate the VE envelopes from a complicated superimposed raw spectrum. The principle of the SP algorithm is analyzed theoretically and verified experimentally. The sensor's RH and temperature response are studied, exhibiting a high sensitivity of about 0.437 nm/%RH and 0.29 nm/°C, respectively. Using a matrix obtained from experiment results, the simultaneous RH and temperature measurement is achieved. Meanwhile, the simple fabrication process, compact size and potential for higher sensitivity makes our proposed structure integrated with the SP algorithm a promising sensor for practical RH and temperature monitoring.

1. Introduction

Monitoring and controlling relative humidity (RH) and temperature is vital in many fields, including agricultural and industrial production, food and electronics manufacturing, and clinical treatment [1–3]. For example, an appropriate humidity level and temperature are essential to a successful surgery and facilitate wound healing and recovery afterward [4]. While there are many schemes for measuring temperature, accurate RH monitoring is more challenging and complex [5]. The increasing demand for RH monitoring has resulted in a variety of sensors being developed, including conventional electronic RH sensors utilizing capacitance, resistance, or conductivity of sensing components, as well as optical fiber RH sensors detecting intensity, wavelength, or phase of the transmitted or reflected light signals [6–8]. Optical fiber sensors (OFSs) offer several advantages over their electronic counterparts, such as their compact size, lightweight, low loss and immunity to electromagnetic interference, which allows them to perform in extremely narrow spaces, electrically noisy environments, and with the capability of multiplexing and remote monitoring [9–12]. Therefore, driven by practical requirements, many optical RH/temperature sensors have attracted considerable interest from researchers worldwide due to their intrinsic properties [8,13].

#498077 https://doi.org/10.1364/OE.498077
Journal © 2023 Received 14 Jun 2023; revised 19 Jul 2023; accepted 31 Jul 2023; published 11 Aug 2023

Optics EXPRESS

Considering the inherent properties of silica, OFSs based on bare silica are not sensitive to RH [14]. Thus, most optical fiber RH sensors are composed of hygroscopic materials, including polyvinyl alcohol (PVA), polycarbonate polymer (PCP), agarose, graphene quantum dots (GQDs), Chitosan, titanium dioxide, and graphene oxide [13,15–19]. The refractive index (RI), volume or electronic mobility of these materials changes with the water molecular absorption, which provides the potential to increase sensitivity. However, standard single-mode fibers (SMFs) strictly confine the light to the core, preventing it from interfacing with the external environment. In order to enhance the overlap between the evanescent field and the functional RH-sensitive materials, different technologies and configurations for RH monitoring have been reported, including tilt fiber Bragg gratings (TFBGs), long period gratings (LPGs), Mach-Zehnder interferometers (MZIs), micro-knots, fiber taper, and side-polished fibers [20–25]. However, these microfabrication processes typically require high-precision processing equipment, such as femtosecond lasers or two-photon polymerization devices. Furthermore, many processing operations, such as tapering, etching, and side-polishing, will significantly reduce the mechanical strength of the sensing head. These factors are not conducive to the mass production or practical application of sensors.

Recently, FPI-based RH sensors have been extensively studied due to their simple structure, high sensitivity, and potential for low-cost production [26–28]. The reflected type enables the application of these sensors to be more user-friendly. In many configurations, the hygroscopic thin film is efficiently manufactured by dip coating, special-designed ultraviolet exposure, and spin-coating or tip-touching process, considerably reducing processing time, difficulty and cost [29–31]. In general, decreasing the length of Fabry-Perot cavities (FPCs) can lead to a significant improvement in sensitivity. L.Chen et al. proposed that reducing the cavity length to 50 μm would result in a 0.13 nm/%RH sensitivity using a single pure chitosan layer [17]. M. Chen et al. have realized an RH sensitivity reached 0.2489 nm/%RH based on a castle style Fabry-Perot microcavity fabricated on the fiber tip using two-photon polymerization [32]. However, further reducing the silica cavity to the micron scale to enhance the sensitivity is not a simple task. Using the Vernier effect (VE) is another effective approach to increase the sensitivity of FPI-type sensors [33,34]. By utilizing two interferometers with comparable free spectral ranges (FSRs), a superimposed reflection spectrum can be generated, which forms an envelope. Compared with the FP fringe, monitoring the shifts in the envelope can significantly amplify the response sensitivity by orders of magnitude. Sensors based on VE have been used to monitor strain, gas pressure, RI, etc [35–37].

Although many RH sensors with VE can achieve high sensitivity, they cannot eliminate the cross-talk of temperature, which is also a shortcoming of many other RH sensors and is inherent to the material [38]. The most common solution is to cascade an FBG to demodulate the temperature cross-talk [39,40]. However, the temperature sensitivity of FBG is only 14 pm/°C, which requires a high-resolution optical spectrum analyzer (OSA) for signal detection [41]. Furthermore, the Bragg wavelength is sensitive to bending and strain applied to the FBG, which limits its application. The intensity of light at specific wavelengths can also be used to calibrate the temperature, but it depends on the long-term stability of the light source and the insertion loss, which is challenging to realize in practice [42].

In this paper, we proposed an inlined FPI for simultaneous measurement of RH and temperature. A section of hollow core Bragg fiber (HCBF) is spliced with a lead-in SMF, and two kinds of polymer films are immobilized at the tip of the HCBF with the help of a microscope. The surfaces of the splicing point and polymer films will form a pair of VE envelops, which helps to improve the sensitivity and demodulate the RH and temperature by using a 2×2 matrix obtained from the experiment results. The two envelopes are demodulated from the superimposed reflection spectrum by using the signal processing (SP) method we proposed. The working principle and effectiveness of the SP algorithm are theoretically analyzed and experimentally verified. The

Optics EXPRESS

simple design, easy fabrication, and high sensitivity make the proposed sensor an excellent candidate for measuring RH and temperature.

2. Working principle

2.1. Fabry-Perot interferometers based on Vernier effect

The schematic diagram of the proposed inline FPI sensor is shown in Fig. 1. The SMF is spliced with a section of hollow core Bragg fiber (HCBF) with a length of several hundred microns. The fabrication process, RI distribution and geometric parameters of the HCBF can be found in our previous work [43]. The end face of the HCBF is coated with two layers of hygroscopic films, which are fabricated to have a significant difference in RI and a varying response to temperature and humidity. As incident light passes through the SMF in the axial direction, it will be partially reflected from the interfaces of materials with different RIs and coupled back to the SMF where interference occurs. Reflection mirrors and light intensities reflected from them are represented as M_i and I_i ($i = 1, 2, 3, 4$), respectively. Based on Fresnel's reflection theory, the reflection coefficients at these interfaces are very low, and multiple reflections of light can be ignored. Therefore, the reflected light intensity I_r can be expressed as follows:

$$I_r = \sum_{i=1}^{4} I_i + 2\sum_{i=2}^{4}\sum_{j=1}^{i-1}\sqrt{I_i I_j}cos\phi_{i,j}, \tag{1}$$

where $cos\phi_{i,j}$ are the phase difference of the light reflected from the mirror M_i and M_j. Here, we set $j<i$, and $cos\phi_{i,j}$ can be calculated as:

$$cos\phi_{i,j} = \phi_{i,j}^{0} + \sum_{m=j}^{i-1}\frac{4\pi n_{m+1,m}L_{m+1,m}}{c}f, \tag{2}$$

where, c and f are the velocity and frequency of light, respectively. $n_{m+1,m}$ and $L_{m+1,m}$ are the RIs and lengths of media between mirror M_{m+1} and M_m. $\phi_{i,j}^{0}$ is the phase variation caused by half-wave loss, whose values depend on the RIs of the media on both sides of the reflecting surface and can either be π or 0. The FPI cavity lengths in our sensor are much longer than the wavelength. Therefore, we can assume that the cavity length differs from the actual length by 1/4 wavelength, thus representing the variation caused by the half-wave loss. In this way, subsequent calculations and discussions can be simplified. Here, we defined spatial frequency as:

$$\omega_{i,j} = \sum_{m=j}^{i-1}\frac{4\pi n_{m+1,m}L_{m+1,m}}{c}. \tag{3}$$

Then, $\phi_{i,j}$ can be approximately expressed as:

$$\phi_{i,j} = \omega_{i,j}f. \tag{4}$$

When only one polymer film exists, I_1, I_2 and I_3 will form a triple-beam interference in the reflection spectrum. The reflected spectrum is simulated. The parameters are set as follows: $I_1 = 5I_2 = 5I_3 = 1$, $n_{2,1} = 1$, $n_{3,2} = 1.7$, $n_{4,3} = 1.3$, $L_{2,1} = 500$ μm, $L_{3,2} = L_{4,3} = 20$ μm. As shown in Fig. 2 (a)(green line), the dense fringes are regulated by an envelope called the VE envelope. The sensor's sensitivity can be significantly increased by monitoring the envelope's shift instead of monitoring the FP fringes. For layer-II, the I_1, I_3 and I_4 can generate another VE-related envelope. However, in the reflection spectrum of our sensor, the two sets of envelopes are superimposed together. Figure 2(c)(green line) is the simulated reflection spectrum of

Optics EXPRESS

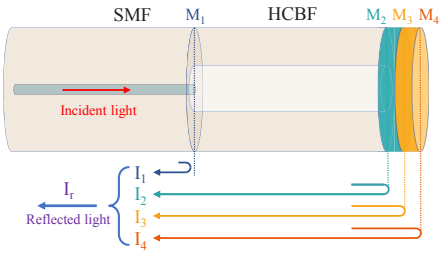

Fig. 1. The schematic diagram of proposed sensor structure.

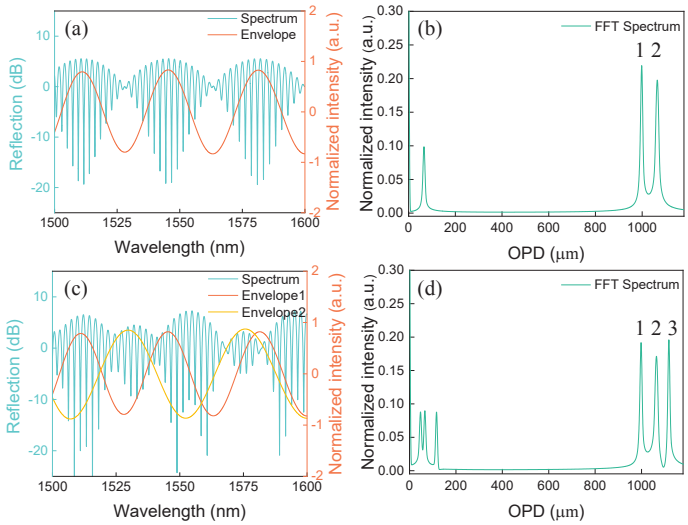

Fig. 2. (a) The simulated reflection spectrum of the sensing probe coated with one polymer layer (green line) and the envelope demodulated using our SP algorithm (orange line) , and (b) related spatial frequency spectrum. (c) The simulated reflection spectrum of the sensing probe coated with two polymer layers (green line) and the envelopes demodulated using our SP algorithm (orange and yellow lines), and (d) related spatial frequency spectrum.

quadruple-beam interference. I_4 is set as 0.2. The complexity of the signal makes it difficult to obtain the individual envelopes from the raw spectra for temperature and humidity sensing.

Therefore, we propose a novel SP method for demodulating valuable information from a complex refraction spectrum. Although $n_{i,j}$ and $I_{i,j}$ vary with wavelength, the fluctuations are small. Thus, they can be approximated as constants within the short bands we tested. According to Eq. (1), the reflected light intensity I_r can be equivalent to a superimposed signal that varies with frequency. Specifically, the first term can be considered the sum of four DC signals. The latter term is the superposition of six AC components, and the spatial frequency can be derived from the Eq. (4).

The flowchart of our SP method is shown in Fig. 3. Firstly, the fast Fourier transform (FFT) is applied to the raw reflection spectrum data to achieve the spatial frequency spectrum. The Fourier transform theory indicates that there are six distinct peaks on the right side of the fundamental spatial frequency. Transverse axes in spatial frequency spectra are converted into optical path differences (OPDs). Peak-1 and peak-2 marked in Fig. 3 correspond to the two sets of interference fringes formed by I_1-I_2 and I_1-I_3, respectively. Secondly, two band-pass filters are designed to obtain the two spatial frequency components. Thirdly, inverse fast Fourier transform (IFFT) is

Optics EXPRESS

conducted to these two spatial frequency components to get the two of the 6 AC signals that make up the superimposed reflected optical spectrum. The two signals are expressed as:

$$s_1 = cos(4\pi n_{2,1}L_{2,1}f/c), \tag{5}$$

$$s_2 = cos[4\pi(n_{2,1}L_{2,1} + n_{3,2}L_{3,2})f/c]. \tag{6}$$

With this process, we can extract the specific spatial frequency components of the complex superposition spectrum. Then, we multiply s_1 by s_2, and get a new components s_3, which can be derived as:

$$\begin{aligned} s_3 &= cos(4\pi n_{2,1}L_{2,1}f/c)cos[4\pi(n_{2,1}L_{2,1} + n_{3,2}L_{3,2})f/c] \\ &= \frac{1}{2}cos[4\pi n_{3,2}L_{3,2}f/c] + \frac{1}{2}cos[4\pi(2n_{2,1}L_{2,1} + n_{3,2}L_{3,2})f/c]. \end{aligned} \tag{7}$$

s_3 is composed of two spatial frequency components. Using a similar method as above, we can extract its low-frequency component and perform an IFFT transform to obtain the signals, which are expressed as:

$$s_4 = cos[4\pi n_{3,2}L_{3,2}f/c]. \tag{8}$$

s_4 is the first VE-related envelope we need to extract. We can get the other envelope using the same method by extracting peak-2 and peak-3.

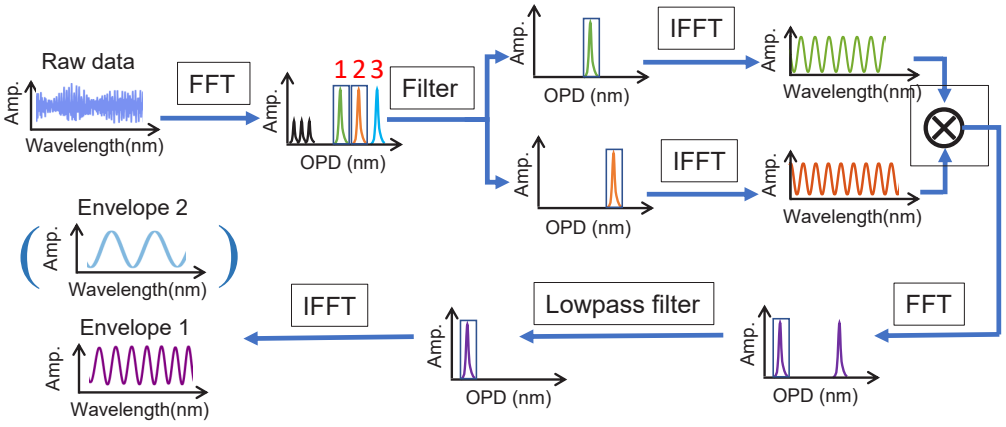

Fig. 3. The flowchart of SP algorithm.

FFT was performed on the two simulated spectra, i.e., Fig. 2(a) and (c), to obtain their spatial frequency spectra, as shown in Fig. 2(b) and (d), respectively. The envelopes demodulated from them are demonstrated in Fig. 2 (a)(orange line) and Fig. 2(c) (orange and yellow lines). In Fig. 2(a), the wavelengths corresponding to the dips in the demodulated curve and the original spectral envelope are matched well. Note that multiple normalization operations are involved in the signal processing to facilitate calculations. As a result, the absolute signal intensities of the original envelope and the extracted curve are different. In our sensing applications, only the positions of these dip wavelengths are utilized to calculate and monitor the measured parameters. Therefore, the calculated envelope provides accurate and effective information from the raw spectral envelope, making it sufficient for sensing applications. Meanwhile, the orange lines in Fig. 2(a) and Fig. 2(c) are identical, indicating that our SP method is capable of extracting expected envelopes from complex superimposed signals. We should note that s_4 is actually a spatial frequency component of I_r, which can be easily observed from Eq. (1). Nevertheless, the period number in the optical spectrum related to s_4 is too few, and the peak corresponding in the spatial frequency spectrum is too close to the vertical axis and nearby peaks. So, it is inaccurate

Optics EXPRESS

to extract s_4 directly from I_r using FFT and filtering. Therefore, it is more effective and reliable method to use our SP algorithm to demodulate it from peak-1 and peak-2.

It should be noted that another envelope can be demodulated from the peak 1-3 in Fig. 2(d) by employing the same method. However, this envelope corresponds to the VE related to the composite film formed by layer-I and layer-II. Compared to the single-layer film, this composite film is thicker, resulting in lower sensitivity when used for sensing applications [30]. Therefore, the envelopes demodulated by peak 1-2 and peak 2-3, rather than peak 1-3, are chosen to ensure the higher sensitivity in our experiment.

The film thicknesses and RIs vary with changes of ambient parameters, resulting in VE-related envelope shifts. Both films are carefully selected, and the fabrication processes are specially designed to ensure their different sensitivities to RH and temperature. By monitoring the shift of the two envelopes, the two ambient parameters are demodulated simultaneously using a matrix obtained through experiments. Meanwhile, the VE contributes to the high response sensitivity.

3. Experiment and discussion

3.1. Sensor fabrication

The fabrication process of our sensing probe is shown in Fig. 4(a-h). A section of homemade HCBF is spliced with the SMF pigtail using a commercial fusing splicer (FITEL S179) operated in manual mode. To minimize the collapse of the air hole in HCBF, the arc power and duration time are carefully adjusted. Specifically, these two parameters were set as 65 and 200 ms, respectively. The loss of the HCBF is much lower than that of the hollow core capillaries of the same size [41]. Meanwhile, compared with the other antiresonant fibers with intricate microstructured cross-sections, the HCBF with cladding of simple structure and substantial thickness mitigates the risk of collapse during fusion, leading to the lower total loss in short fiber length [44]. The HCBF is cut to a length of 870 μm with the help of a microscope. The fiber tip is then vertically dipped into a Chitosan solution for approximately 3 seconds. The Chitosan solution with a concentration of 1% was prepared in our lab, and the process can be found in previous work [28]. After being coated with Chitosan, the structure is placed in an environmental test chamber (ETC) to evaporate water. Afterward, an SMF with a small droplet of ultraviolet optical adhesive (UVOA) (NOA 170, Norland Products Inc) at its end-face is aligned with the HCBF. The UVOA was transferred to the Chitosan film in a small amount by tip touching. The UVOA will cross-link with Chitosan and form a composite film after exposing to ultraviolet light (UVL) for about 1 hour. The film is referred to as layer-I. Next, an SMF with another kind of UVOA (NOA 1315, Norland Products Inc) at its tip is aligned to layer-I and maintains contact.

Meanwhile, the UVL cures the whole structure from the left side for about 2 seconds. Then, the HCBF moves away from the right SMF. The exposure time is too short, and the liquid adhesive is partially but not entirely cured. The left side of layer-II is more exposed than the right side and sticks more firmly. Therefore, layer-II will separate from the SMF at the right surface. The sensing structure was then cured for approximately one hour under UVL. The schematic of our sensing structure is shown in Fig. 4(i). The RIs of the UVOA-I and UVOA-2 used here are about 1.7 and 1.33, respectively. According to the Fresnel formula, the theoretically calculated reflectivities at the M_2, M_3 and M_4 are about 6.72%, 1.49% and 2.01%, respectively. Meanwhile, our fabrication process ensures that the surfaces of layer-I and layer-II are smooth, thereby providing sufficient reflection coefficients at these mirrors, which is crucial to effectively demodulate the envelopes from the reflected spectrum of our sensor.

During the fabrication process, the reflection spectra were collected. The schematic diagram of the experimental setup used here is illustrated in Fig. 5. Light is emitted from a broadband source (BBS), and reflected light is collected by an OSA after passing through the optical circulator (OC). The reflection spectrum in the fabrication process with only layer-I coated at the HCBF is shown in Fig. 6(a)(green line). A dense fringe is formed by the interference between the I_1, I_2 and I_3.

Optics EXPRESS

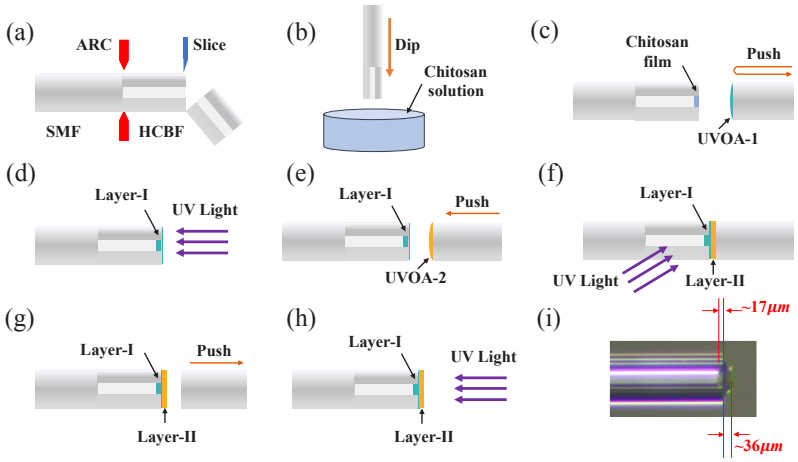

Fig. 4. (a)-(h)The schematic diagrams of the fabrication processes of our proposed sensor. (i) The microscopy image of the fabricated sensing probe.

Meanwhile, the fringes are modulated by an envelope, which is formed due to the VE. Figure 6(b) illustrates the results of analyzing the optical spectrum using the FFT. Two distinct peaks are observed at the OPD of 1743 μm and 1803 μm, which correspond to the interferences formed by I_1-I_2 and I_1-I_3, respectively. It is noted that the peaks associated with I_2-I_3 are insignificant because both intensities of the two beams are low. As shown in Fig. 6(a)(orange line), the VE envelope can be calculated using our SP method. The dip positions are consistent with the raw optical spectrum.

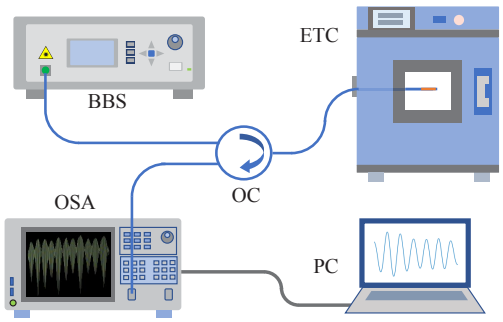

Fig. 5. Experimental setup for relative humidity and temperature response test.

The reflection spectrum of our sensor with two polymer layers is shown in Fig. 6(c). The reflection spectrum is too complicated to identify the VE envelope. Our SP algorithm was conducted to analyze the raw spectrum. Fig. 6(d) shows the spatial frequency spectrum of our sensors, which contains four dominant peaks. Two of them are located at the same OPD as in Fig. 6(b). After coating with layer-II, the intensity of peak-2 decreased, as the material's RI on the right side of M_3 increased from 1 to 1.33, resulting in a significant reduction in reflectivity of M_3. Furthermore, the outer surface of layer-II, i.e., M_4, partially reflects light, which interferes with I_1 to form peak-3. The envelopes demodulated from peak 1-2 and peak 2-3 by our SP method are shown in Fig. 6(c) as the orange and yellow lines, respectively. The envelope-1 is consistent with that shown in Fig. 6(a). During the process of making layer-II, layer-I was squeezed slightly, resulting in some offset between the two envelopes. Noted that the amplitude

Optics EXPRESS

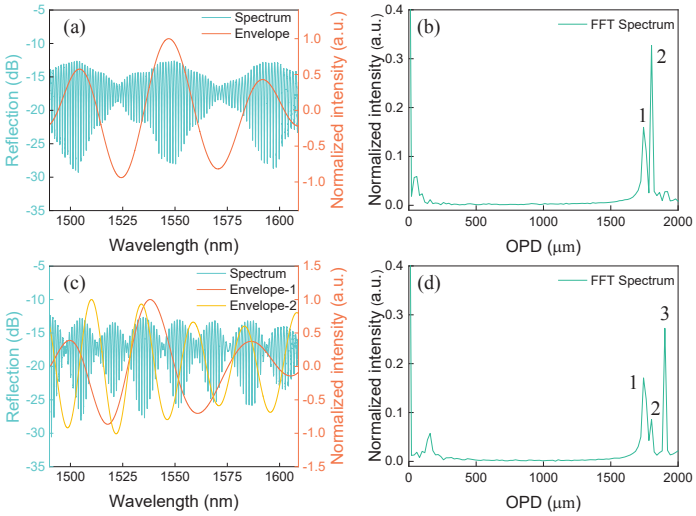

Fig. 6. (a) The measured reflection spectrum of the sensing probe coated with one polymer layer (green line) and the envelope demodulated using our SP algorithm (orange line) , and (b) related spatial frequency spectrum. (c) The measured reflection spectrum of the sensing probe coated with two polymer layers (green line) and the envelopes demodulated using our SP algorithm (orange and yellow lines), and (d) related spatial frequency spectrum.

of the extracted envelope varies with wavelength, which remains stable in the simulation results shown in Fig. 2(a). During simulation, the spectrum is an ideal triple-beam interference result, and the reflected light intensities at different wavelengths are the same. However, in practical applications, the reflection coefficients vary at different wavelengths. At the same time, the excited higher-order modes in HCBF will also be guided and reflected from the polymer films. Therefore, the reflected spectrum is not a pure triple-beam interference, and other beams have involved in the reflected spectrum, as illustrated in Fig. 6(a) (green line). Consequently, there are fluctuations in peak intensities observed in the extracted envelope. Combining the results shown in Fig. 2 and Fig. 6, we have demonstrated theoretically and experimentally that our SP approach is convenient, accurate, and effective.

3.2. *Relative humidity response*

The experiments for RH and temperature response of our sensor were tested using the same equipment as shown in Fig. 5. Sensing probes were fixed in silica tubes and placed in the ETC for testing. The temperature in the chamber was set at 20 °C, and the RH value was increased from 50% to 85% with an interval of 5% RH. After reaching the set value and before data acquisition, the RH was stabilized for approximately 15 minutes to minimize fluctuations. The spectra evolution during the RH-increasing period is shown in Fig. 7(a). The SP method was conducted to the raw spectra to demodulate the two EV envelops, shown in Fig. 7(b) and (c). Both envelopes exhibit a redshift when RH is increased, while their response sensitivities are different. Fig. 7(d) illustrates the calculated relationship between wavelength shifts at one minimal around 1550 nm and RH values of envelope-1. Linear fitting was carried out, where the slope is about 0.4344 *nm*/% RH. For envelope-2, the wavelength shift of the envelope also exhibits a linear relationship with RH, as shown in Fig. 7(e). The sensitivity is about 39.79 pm/% RH, which is much lower than that of envelope-1. This is attributed to the difference between the two films in composition and thickness.

Optics EXPRESS

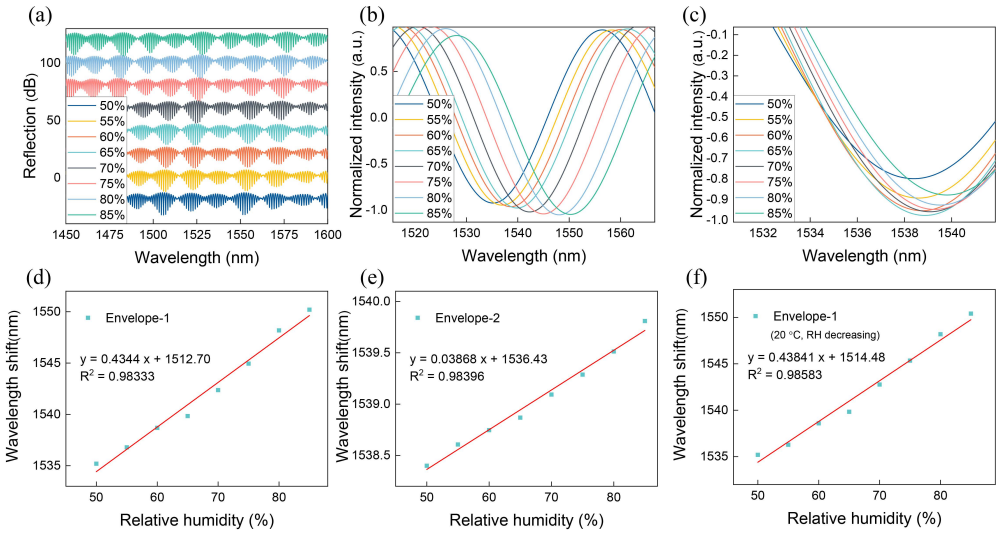

Fig. 7. (a) The raw reflection spectra under 20°C with RH changing from 50% to 85%, and (b-c) demodulated envelopes in this process. (d-e) The wavelength shift of envelope-1 and envelope-2 as functions of RH. (f) The wavelength shift of envelope-1 under 20°C with RH changing from 85% to 50%.

Following the RH-increasing period, the RH value was decreased in the same step from 85% to 50%. We take the RH response of envelope-1 as an example to discuss the repeatability of our sensor. The relationship between dip wavelength and RH at the RH-decreasing process is shown in Fig. 7(f), and linear fitting was conducted. It can be seen that the sensitivity obtained by the linear fit matches well in both processes of increasing and decreasing humidity, demonstrating our sensor's good repeatability. Following this, the RH response experiments were repeated at temperatures of about 30 °C and 40 °C, respectively. The relationship between dip wavelength and RH during these processes are shown in Fig. 8(a) and (b), respectively. The linear fitting is conducted, and the slope values in these three temperatures are consistent, which means that the RH response sensitivity of our sensor is almost the same at different temperatures. It provides a prerequisite for the subsequent simultaneous measurement of RH and temperature.

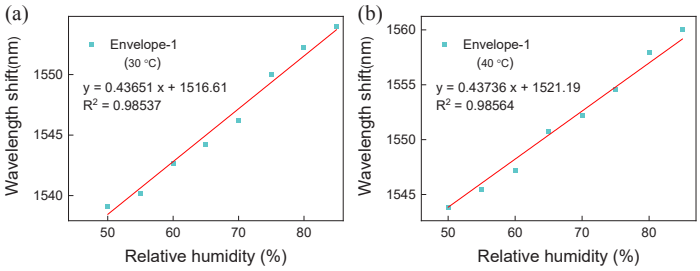

Fig. 8. The wavelength shift of envelope-1 with RH changing from 50% to 85% under (a) 30°C and (b) 40°C.

3.3. *Temperature response*

The temperature response of our sensor is carried out by setting the RH value at about 46%. The temperature in the chamber was increased from 26 °C to 46 °C with a step of 2 °C. The

Optics EXPRESS

temperature at each step was also kept for about 15 minutes after reaching the expected value. The reflection spectra collected during this process are shown in Fig. 9(a). By using our SP methods, the two VE envelopes are extracted from the raw spectra, and the evolution of each envelope are shown in Fig. 9(b) and (c), respectively. With the increase in temperature, envelope-1 shifts to the longer wavelength, while envelope-2 shifts to the shorter wavelength. The variations of the two envelopes at around 1550 nm are individually shown in Fig. 10(a) and (b), respectively. The sensitivity of two envelopes are about 296.27 pm/°C and -129.33 pm/°C.

3.4. Discussion

When the RH and temperature applied to the sensing probe vary simultaneously, the shift of envelop-1 and envelop-2 can be expressed as :

$$\Delta\lambda_1 = S_{11} \cdot \Delta RH + S_{21} \cdot \Delta T, \tag{9}$$

$$\Delta\lambda_2 = S_{12} \cdot \Delta RH + S_{22} \cdot \Delta T, \tag{10}$$

where S_{11}, S_{21}, S_{12} and S_{22} are the sensitivity obtained by linear fitting in the RH and temperature response test. Therefore, the RH and temperature values can be calculated by the following matrix:

$$\begin{bmatrix} \Delta RH \\ \Delta T \end{bmatrix} = \frac{1}{S_{11}S_{22} - S_{21}S_{12}} \begin{bmatrix} S_{22} & -S_{21} \\ -S_{12} & S_{11} \end{bmatrix} \begin{bmatrix} \Delta\lambda_1 \\ \Delta\lambda_2 \end{bmatrix}. \tag{11}$$

.

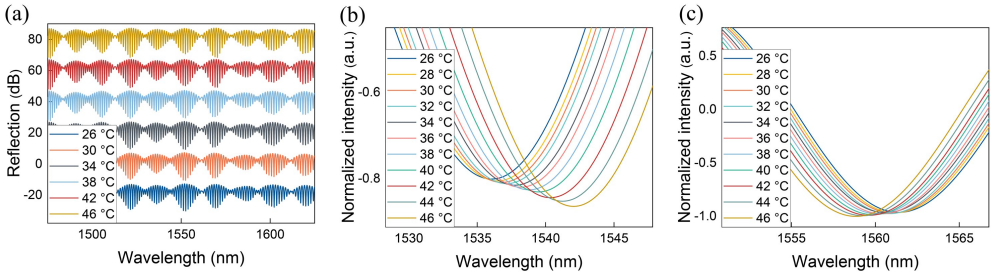

Fig. 9. (a) The raw reflection spectra under 45%RH with temperature changing from 26°C to 46°C, and (b-c) demodulated envelopes in this process.

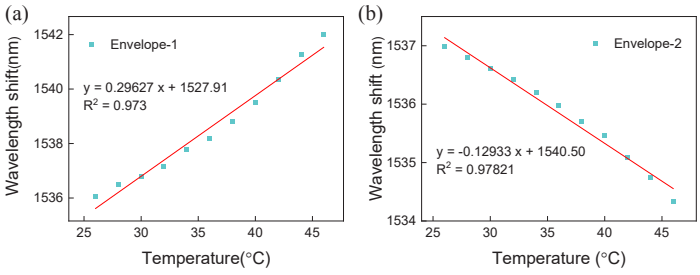

Fig. 10. The wavelength shift of envelope-1 and envelope-2 as functions of temperature under 46%RH.

Optics EXPRESS

Submitting the slope values we obtained, then the RH and temperature can be achieved simultaneously by the EV envelopes' shifts:

$$\begin{bmatrix} \Delta RH \\ \Delta T \end{bmatrix} = \frac{1}{67928.33} \begin{bmatrix} 129.33 & 296.27 \\ 38.66 & -436.67 \end{bmatrix} \begin{bmatrix} \Delta\lambda_1 \\ \Delta\lambda_2 \end{bmatrix}. \tag{12}$$

The units of ΔRH, ΔT and $\Delta\lambda$ are %, °C and pm, respectively. Due to the limitation of our experimental setup, the simultaneous and stable control of RH and temperature in a larger range is hard to achieve. However, according to previous published works, linear response in a wider range of RH and temperature using Chitosan and UVOA have been reported and demonstrated that can endorse this work [29,30].

Fluctuations in temperature are frequently concomitant with changes in humidity in practical sensing applications. High-sensitivity RH sensors are typically manufactured using hygroscopic materials, including PVA, Chitosan, UVOA, agarose, and graphene oxide. The RIs and volumes of these materials typically change with temperature. Therefore, the lack of temperature compensation ability will significantly compromise the reliability and stability of humidity sensors due to temperature cross-talk. Our proposed sensor offers an solution that enables dual parametric sensing using a single sensing probe. In our sensor, both surfaces of layer-I can be made smooth with high reflective coefficients, thanks to our two-step film fabrication method. The outer surface of layer-II is flat due to the step-by-step curing process. Because of the difference in RI between layer-I and layer-II, the reflectivity of the interface between them are sufficient. This is the basis for using our algorithm to extract the two envelopes. Additionally, the material selection ensures that the two layers respond differently to temperature and RH. Combining these designs could demodulate the temperature and achieve dual parametric sensing.

Our SP algorithm not only be capable of demodulating information that cannot be directly obtained from the spectrum, such as multiple Vernier effect envelopes, but also assist to achieve better accuracy and lower experimental error compared to traditional demodulation methods. Most optical fiber RH sensors rely on a single dip (or peak) to realize monitoring, utilizing the intensity variability or shifts of this specific wavelength. Likewise, in the conventional VE-based RH scheme, the envelope is also extracted by connecting the extrema points of the interference fringes. The sensing information in these sensors is obtained from a very narrow waveband located around the valleys of the fringes or envelopes. As a result, random low-frequency noise or disturbances can have a more significant impact on sensing results. In contrast, the VE envelopes of our sensor are demodulated from the entire spectrum data collected. The envelope is computed by applying two high-frequency signals, such as peak-1 and peak-2, which enables the extraction of pure multi-beam interferences without any low-frequency or random disturbances. As a result, our sensors exhibit a low error rate and high accuracy.

Using the Vernier effect is an effective method for increasing the RH sensitivity of an FPI-based sensor, as demonstrated by our sensor. The fabrication process of the sensor involves only one microscope and a pair of 3D stages, which are simple and low-cost. Despite this simplicity, the achieved sensitivities are comparable to, and even superior to, those obtained using more complex experimental equipment. It should be noted that the sensitivity is negatively correlated with the thickness of the layers in our proposed sensor and several early reported sensor structures similar to ours [28,30]. The amount of UVOA can be reduced by spin coating, or the SMF used for tip touching can be replaced by a thin fiber with a smaller outer diameter. This requires the use of spin coaters or tapering station, which increases the cost. Therefore, we do not discuss it extensively in our low-cost sensors. Nevertheless, there is a potential for application in many applications where increased sensitivity is required and costs can be raised appropriately.

Optics EXPRESS

4. Conclusion

In conclusion, a novel sensor is proposed and experimentally demonstrated for simultaneous measurement of RH and temperature. The sensor fabrication processes are detailedly studied and optimized, which contributes to the high reflectivity of each surface and generates the VE envelopes for enhanced sensing capability. A well-designed SP algorithm is introduced and applied to extract the envelopes from the raw spectrum. RH and temperature can be measured simultaneously with high sensitivity using an experiment-derived matrix. The good repeatability has been experimentally verified in the process of RH increasing or decreasing at different temperatures. Besides, the sensor shows various advantages of compact size, low cost, easy making and convenient reflective probe, indicating it more competitive in actual applications.

Funding. Hong Kong Research Grants Council (GRF 15217620, 15227321)National Natural Science Foundation of China (62205297); Shenzhen Municipal Science and Technology Innovation Commission (P0034676).

Disclosures. The authors declare no conflicts of interest.

Data Availability. The data that support this study are available from the corresponding author upon reasonable request.

References

1. M. H. Mahmood, M. Sultan, and T. Miyazaki, "Significance of temperature and humidity control for agricultural products storage: overview of conventional and advanced options," Int. J. Food Eng. **15** (2019).
2. Z. Chen and C. Lu, "Humidity sensors: a review of materials and mechanisms," Sensor Lett. **3**(4), 274–295 (2005).
3. B. Song, M. H. Azarian, and M. G. Pecht, "Effect of temperature and relative humidity on the impedance degradation of dust-contaminated electronics," J. Electrochem. Soc. **160**(3), C97–C105 (2013).
4. C. L. Lim, C. Byrne, and J. K. Lee, "Human thermoregulation and measurement of body temperature in exercise and clinical settings," Ann. Acad. Med. Singapore **37**(4), 347–353 (2008).
5. B. A. Kuzubasoglu and S. K. Bahadir, "Flexible temperature sensors: A review," Sens. Actuators, A **315**, 112282 (2020).
6. T. Blank, L. Eksperiandova, and K. Belikov, "Recent trends of ceramic humidity sensors development: A review," Sens. Actuators, B **228**, 416–442 (2016).
7. C. Lv, C. Hu, J. Luo, S. Liu, Y. Qiao, Z. Zhang, J. Song, Y. Shi, J. Cai, and A. Watanabe, "Recent advances in graphene-based humidity sensors," Nanomaterials **9**(3), 422 (2019).
8. Y. Peng, Y. Zhao, M.-Q. Chen, and F. Xia, "Research advances in microfiber humidity sensors," Small **14**, 1800524 (2018).
9. P. Lu, N. Lalam, M. Badar, B. Liu, B. T. Chorpening, M. P. Buric, and P. R. Ohodnicki, "Distributed optical fiber sensing: Review and perspective," Appl. Phys. Rev. **6**(4), 041302 (2019).
10. R. Min, Z. Liu, L. Pereira, C. Yang, Q. Sui, and C. Marques, "Optical fiber sensing for marine environment and marine structural health monitoring: A review," Opt. Laser Technol. **140**, 107082 (2021).
11. A. G. Leal-Junior, C. A. Diaz, L. M. Avellar, M. J. Pontes, C. Marques, and A. Frizera, "Polymer optical fiber sensors in healthcare applications: A comprehensive review," Sensors **19**(14), 3156 (2019).
12. A. K. Sharma, A. K. Pandey, and B. Kaur, "A review of advancements (2007–2017) in plasmonics-based optical fiber sensors," Opt. Fiber Technol. **43**, 20–34 (2018).
13. Y. Zhao, R.-J. Tong, M.-Q. Chen, and F. Xia, "Relative humidity sensor based on hollow core fiber filled with gqds-pva," Sens. Actuators, B **284**, 96–102 (2019).
14. S. Pevec and D. Donlagic, "Miniature all-silica fiber-optic sensor for simultaneous measurement of relative humidity and temperature," Opt. Lett. **40**(23), 5646–5649 (2015).
15. Y. Wang, C. Shen, W. Lou, and F. Shentu, "Fiber optic humidity sensor based on the graphene oxide/pva composite film," Opt. Commun. **372**, 229–234 (2016).
16. J. Mathew, Y. Semenova, and G. Farrell, "Relative humidity sensor based on an agarose-infiltrated photonic crystal fiber interferometer," IEEE J. Sel. Top. Quantum Electron. **18**(5), 1553–1559 (2012).
17. L. H. Chen, T. Li, C. C. Chan, R. Menon, P. Balamurali, M. Shaillender, B. Neu, X. M. Ang, P. Zu, W. C. Wong, and K. C. Leong, "Chitosan based fiber-optic fabry–perot humidity sensor," Sens. Actuators, B **169**, 167–172 (2012).
18. D. Zhang, X. Zong, Z. Wu, and Y. Zhang, "Ultrahigh-performance impedance humidity sensor based on layer-by-layer self-assembled tin disulfide/titanium dioxide nanohybrid film," Sens. Actuators, B **266**, 52–62 (2018).
19. S. Borini, R. White, D. Wei, M. Astley, S. Haque, E. Spigone, N. Harris, J. Kivioja, and T. Ryhanen, "Ultrafast graphene oxide humidity sensors," ACS Nano **7**(12), 11166–11173 (2013).
20. Y. Miao, B. Liu, H. Zhang, Y. Li, H. Zhou, H. Sun, W. Zhang, and Q. Zhao, "Relative humidity sensor based on tilted fiber bragg grating with polyvinyl alcohol coating," IEEE Photonics Technol. Lett. **21**(7), 441–443 (2009).
21. T. Venugopalan, T. L. Yeo, T. Sun, and K. T. Grattan, "Lpg-based pva coated sensor for relative humidity measurement," IEEE Sensors J. **8**(7), 1093–1098 (2008).

Optics EXPRESS

22. M. Shao, X. Qiao, H. Fu, H. Li, J. Zhao, and Y. Li, "A mach–zehnder interferometric humidity sensor based on waist-enlarged tapers," Opt. Lasers Eng. **52**, 86–90 (2014).
23. Y.-G. Han, "Relative humidity sensors based on microfiber knot resonators—a review," Sensors **19**(23), 5196 (2019).
24. H. Liu, Y. Miao, B. Liu, W. Lin, H. Zhang, B. Song, M. Huang, and L. Lin, "Relative humidity sensor based on s-taper fiber coated with sio 2 nanoparticles," IEEE Sensors J. **15**(6), 3424–3428 (2015).
25. X. Wang, G. Farrell, E. Lewis, K. Tian, L. Yuan, and P. Wang, "A humidity sensor based on a singlemode-side polished multimode–singlemode optical fibre structure coated with gelatin," J. Lightwave Technol. **35**(18), 4087–4094 (2017).
26. M. R. Islam, M. M. Ali, M.-H. Lai, K.-S. Lim, and H. Ahmad, "Chronology of fabry-perot interferometer fiber-optic sensors and their applications: a review," Sensors **14**(4), 7451–7488 (2014).
27. J. Shi, D. Xu, W. Xu, Y. Wang, C. Yan, C. Zhang, D. Yan, Y. He, L. Tang, W. Zhang, T. Liu, and J. Yao, "Humidity sensor based on fabry–perot interferometer and intracavity sensing of fiber laser," J. Lightwave Technol. **35**(21), 4789–4795 (2017).
28. Y. Wang, Y. Yan, Z. Lian, D. Chen, A. P. T. Lau, and C. Lu, "Fabry–perot interferometers for highly-sensitive multi-point relative humidity sensing based on vernier effect and digital signal processing," Opt. Express **30**(22), 39946–39960 (2022).
29. C. Wang, G. Yan, Z. Lian, X. Chen, S. Wu, and S. He, "Hybrid-cavity fabry-perot interferometer for multi-point relative humidity and temperature sensing," Sens. Actuators, B **255**, 1937–1944 (2018).
30. C. Zhou, Q. Zhou, B. Wang, J. Tian, and Y. Yao, "High-sensitivity relative humidity fiber-optic sensor based on an internal–external fabry–perot cavity vernier effect," Opt. Express **29**(8), 11854–11868 (2021).
31. C. Lang, Y. Liu, K. Cao, Y. Li, and S. Qu, "Ultra-compact, fast-responsive and highly-sensitive humidity sensor based on a polymer micro-rod on the end-face of fiber core," Sens. Actuators, B **290**, 23–27 (2019).
32. M.-Q. Chen, Y. Zhao, H.-M. Wei, C.-L. Zhu, and S. Krishnaswamy, "3d printed castle style fabry-perot microcavity on optical fiber tip as a highly sensitive humidity sensor," Sens. Actuators, B **328**, 128981 (2021).
33. A. D. Gomes, H. Bartelt, and O. Fraz ao, "Optical vernier effect: recent advances and developments," Laser Photonics Rev. **15**, 2000588 (2021).
34. Y. Chen, L. Zhao, S. Hao, and J. Tang, "Advanced fiber sensors based on the vernier effect," Sensors **22**(7), 2694 (2022).
35. T. Nan, B. Liu, Y. Wu, J. Wang, Y. Mao, L. Zhao, T. Sun, and J. Wang, "Ultrasensitive strain sensor based on vernier-effect improved parallel structured fiber-optic fabry-perot interferometer," Opt. Express **27**(12), 17239–17250 (2019).
36. H. Lin, F. Liu, H. Guo, A. Zhou, and Y. Dai, "Ultra-highly sensitive gas pressure sensor based on dual side-hole fiber interferometers with vernier effect," Opt. Express **26**(22), 28763–28772 (2018).
37. J. Li, M. Zhang, M. Wan, C. Lin, S. Huang, C. Liu, Q. He, X. Qiu, and X. Fang, "Ultrasensitive refractive index sensor based on enhanced vernier effect through cascaded fiber core-offset pairs," Opt. Express **28**(3), 4145–4155 (2020).
38. J. Ascorbe, J. M. Corres, F. J. Arregui, and I. R. Matias, "Recent developments in fiber optics humidity sensors," Sensors **17**(4), 893 (2017).
39. Y. Wang, Q. Huang, W. Zhu, and M. Yang, "Simultaneous measurement of temperature and relative humidity based on fbg and fp interferometer," IEEE Photonics Technol. Lett. **30**(9), 833–836 (2018).
40. Y. Qi, C. Jia, L. Tang, M. Wang, Z. Liu, and Y. Liu, "Simultaneous measurement of temperature and humidity based on fbg-fp cavity," Opt. Commun. **452**, 25–30 (2019).
41. Y. Wang, J. Tao, W. Yuan, Z. Lian, Q. Ling, D. Chen, Z. Yu, and C. Lu, "Hollow core bragg fiber integrated with regenerate fiber bragg grating for simultaneous high temperature and gas pressure sensing," J. Lightwave Technol. **39**(17), 5643–5649 (2021).
42. C. He, S. Korposh, R. Correia, L. Liu, B. R. Hayes-Gill, and S. P. Morgan, "Optical fibre sensor for simultaneous temperature and relative humidity measurement: Towards absolute humidity evaluation," Sens. Actuators, B **344**, 130154 (2021).
43. Y. Wang, G. Yan, Z. Lian, C. Wu, and S. He, "Liquid-level sensing based on a hollow core bragg fiber," Opt. Express **26**(17), 21656–21663 (2018).
44. F. Poletti, "Nested antiresonant nodeless hollow core fiber," Opt. Express **22**(20), 23807–23828 (2014).